science.sciencemag.org/content/369/6501/289/suppl/DC1

# Supplementary Materials for

## Second critical point in two realistic models of water

Pablo G. Debenedetti*†, Francesco Sciortino†, Gül H. Zerze†

*Corresponding author. Email: pdebene@princeton.edu
†These authors contributed equally to this work.

Published 17 July 2020, *Science* **369**, 289 (2020)
DOI: 10.1126/science.abb9796

**This PDF file includes:**

## Materials and Methods

Simulation Methods

Molecular dynamics simulations of water were performed with GROMACS (*43* ,*44*) version 5.1.4, both in the isothermal-isochoric (NVT) and the isothermal isobaric (NPT) ensembles. In both cases, a leap-frog integrator with a time step of 2 fs was used. Electrostatic interactions were calculated using the particle-mesh Ewald method (*45*) with a real space cutoff distance of 0.9 nm. A 0.9 nm cutoff distance was also used for the van der Waals interactions. A Nose-Hoover thermostat with a characteristic time of about 10 ps implemented the constant temperature condition. In the NPT simulations, pressure was maintained via an isotropic Parrinello-Rahman barostat with time scale around 20 ps. Molecular constraints were implemented with the LINCS algorithm of order 6. Cubic systems (with periodic boundary conditions) of size 300, 500 and 1000 were studied in the (N, P, T) ensemble. A cubic system of 36,424 molecules at density 1.012 g/cm$^3$ (also with periodic boundary conditions) for TIP4P/2005 and one of 10,000 molecules at density 1.015 g/cm$^3$ for TIP4P/Ice were studied in the (N, V, T) ensemble. The temperatures and duration of the NVT simulations are presented in Table S4. The studied state points and the length of each run for NPT simulations are listed in the following two tables, one for TIP4P/2005 (Table S1) and one for TIP4P/Ice (Table S2).

The density of 1.012 g/cm$^3$ is the critical density estimated by Abascal and Vega (*46*) for TIP4P/2005. We note that the difference between this estimate and a more recent estimate of critical density with two-state fit (1.017 g/cm$^3$) (*47*) is less than 0.5%. As we had to fix the density at the critical density, we decided to use one of the close estimates mentioned above. Subsequently, our concomitantly running smaller box simulations yielded an average critical density of $\rho_c = 1.030 \pm 0.006$ g/cm$^3$ (the average is calculated from the estimates at different sizes given in Table S3), which is ca. 1% different than the density we used. Given the flat nature of the phase coexistence curve near the critical point, we consider these densities to be nearly equivalent for the purpose of estimating the scaling of critical fluctuations, especially for temperatures not too close to the critical temperature (*48*, *49*). For TIP4P/Ice, our concomitantly running smaller box simulations yielded an average critical density of $\rho_c = 1.015 \pm 0.002$ g/cm$^3$ (the average is calculated from the estimates at different sizes given in Table S3) so we fix the density at $\rho_c = 1.015$ for the $N = 10{,}000$ system.

The $N = 36{,}424$ and $N$=10,000 systems are equilibrated at each temperature, independently, monitoring the time dependence of the potential energy. For TIP4P/2005, we treat the initial 2 $\mu$s and 0.5$\mu$s as equilibration for temperatures between 179 and 185 K, and for temperatures between 190 and 300 K, respectively. For TIP4P/Ice, we treat the initial 1 $\mu$s as equilibration. The equilibration period is excluded from the analysis.

## Supplementary Text

Multiple Histograms

The idea of the Multiple Histogram method (*50* ,*51*) is to merge information from several independent simulations to generate the best estimate of the density of states $\boldsymbol{\Omega}$. It can be used in any ensemble. In the NPT ensemble the partition function $Z(P_i, \beta_i)$ depends on the temperature $T_i$ (or equivalently on $\beta_i = 1/k_B T_i$ where $k_B$ is the Boltzmann constant) and on the pressure $P_i$ as independent variables, and can be written as:

$$\mathcal{Z}(P_i, \beta_i) = \sum_V \sum_E \Omega(V, E)\, e^{-\beta_i(E+P_iV)} = e^{-\beta_i G(P_i,\beta_i)}$$

where $\boldsymbol{\Omega}(E,V)$ is a function of the system energy $E$ and volume $V$ (assumed to be discrete variables calculated with some predefined mesh size). $G(P_i, \beta_i)$ is the associated Gibbs potential.

To find the best estimate of $\boldsymbol{\Omega}(E,V)$, $R$ simulations at different $(T_i, P_i)$ ($i$ = 1, ..., $R$) are performed, saving $N_i$ equally spaced configurations. The histogram $H_i(E, V)$ of sampled $E$ and $V$ in simulation $i$ provides an estimate ($\boldsymbol{\Omega}_i$) of $\boldsymbol{\Omega}(E, V)$,

$$\Omega_i(E,V)\, e^{-\beta_i(E+P_iV)}\, e^{\beta_i G(P_i,\beta_i)} = \frac{H_i(E,V)}{N_i} \longrightarrow \Omega_i(E,V) = \frac{H_i(E,V)}{N_i} e^{+\beta_i(E+P_iV)}\, e^{-\beta_i G(P_i,\beta_i)}.$$

Each of the $R$ simulations provides an estimate over a portion of $E$ and $V$ values, the ones preferentially sampled at the selected $\beta_i$ and $P_i$. The optimal $\boldsymbol{\Omega}(E, V)$ is written as a linear combination, with weight factors $\omega_i(E, V)$ as

$$\Omega(E,V) = \sum_{i=1}^{R} \omega_i(E,V)\Omega_i(E,V) = \sum_{i=1}^{R} \omega_i(E,V) \frac{H_i(E,V)}{N_i} e^{+\beta_i(E+P_iV)}\, e^{-\beta_i G(P_i,\beta_i)}.$$

This expression can be optimized by minimizing the variance of $\boldsymbol{\Omega}(E, V)$, subject to the constraint $\sum_i \omega_i(E,V) = 1$. The final result is (*50*)

$$\Omega(E,V) = \frac{\sum_{i=1}^{R} H_i(E,V)}{\sum_{i=1}^{R} e^{-\beta_i(E+P_iV)}\, e^{\beta_i G(P_i,\beta_i)} N_i} \tag{S1}$$

where, for consistency,

$$e^{-\beta_i G(P_i,\beta_i)} = \sum_V \sum_E e^{-\beta_i(E+P_iV)}.$$

The last two equations are solved self-consistently in an iterative way. Less than 50 iterations are usually sufficient to reach convergence.

Once $\boldsymbol{\Omega}(E,V)$ is known, it becomes possible to predict the probability of observing the system with energy $E$ and volume $V$ at any generic $T$ and $P$ as (*52*):

$$P(E,V,\beta,P) = \frac{\Omega(E,V)e^{-\beta(E+PV)}}{\sum_V \sum_E \Omega(E,V)e^{-\beta(E+PV)}}. \tag{S2}$$

To provide an indication of the quality of the numerical data and of the ability of the histogram reweighting technique to combine different sets of data (at different T and P) in order to generate an optimal density of states, in Fig. S1 we present a comparison of density histograms calculated directly from the simulations with those recalculated from Eq. S2 (i.e., from histogram reweighting) at the same state points.

Fit to the Ising Universality Class

To provide evidence that the liquid-liquid critical point belongs to the 3D-Ising universality class, we compare the spectrum of density and energy fluctuations with the known asymptotic expression for the order parameter $M$ for the Ising model, where $M$ is the system's magnetization. A convenient expression, which can be used in a non-linear fit procedure is provided in Ref. (*53*). It states that at the critical point, a surprisingly good approximation to $P_{Ising}(M)$, the probability that the system has magnetization $M$, is

$$P_{Ising}(M) = A\, exp\{-(\frac{M^2}{M_0^2} - 1)^2 (a\frac{M^2}{M_0^2} + c)\} \quad \text{(S3)}$$

where $a = 0.158$ and $c = 0.776$, $M_0$ is a scale-dependent parameter that controls the variance of the distribution, and $A$ is a normalization factor, such that $\int P_{Ising}(M)dM = 1$.

In the case of a fluid, the order parameter $M$ can be identified with a linear combination of density $\rho$ and energy per particle $E$ (*32*). A non-linear fit procedure can be exploited to find the $T$, $P$ and field mixing parameter $s$ for which the fluctuations of $M$ match the theoretically predicted ones (Eq. S3).

More specifically, we implement the following procedure: for any state point ($T$, $P$), histogram reweighting (see Eqs. S1-S2) is used to generate the distribution of $E$ and $\rho$ and the associated distribution $P(t)$ of $t \equiv \rho + sE$. The variable $t$ is then shifted by its average value $\bar{t}$ and scaled according to the variance $\sigma_t$ as

$$M \equiv \frac{(t-\bar{t})}{\sigma_t} \quad \text{(S4)}$$

to generate a new variable $M$ whose distribution has by construction zero average and unitary variance.

A comparison of $P(M)$ with the theoretical $P_{Ising}(M)$, also transformed in its normalized and unit variance form ($M_0 = 1.1341655$) allows us to calculate the least squared error and use this quantity in the MINUIT package in the search for the optimal $T$, $P$ and $s$, thus yielding numerical estimates of $T_c$, $P_c$. $\rho_c$ is the average density calculated at the state point $T_c$, $P_c$.

Ising Fit for N=500 and N=1000 Systems

We have also studied N=500 and N=1000 systems to reproduce the Ising behavior observed in the N=300 system.

Fig. S6 compares the behavior of TIP4P/2005 (top) and TIP4P/Ice (bottom) with the ideal Ising distribution for all small sizes studied in this work.

Table S3 shows the results of the fit ($T_c$, $P_c$, $s$, $\rho_c$) for all studied system sizes. The table also reports the critical $T$ evaluated from the temperature dependence of $S(0)$ and $\xi$ for the $N = 36{,}424$ system for TIP4P/2005 (see Eqs. 2,3,5 and Fig. 3 in main text). The size dependence of the critical parameters is well within the numerical error. The average of the values over the three smaller sizes provides the best estimate of the critical parameters, and is the value reported in the main manuscript for each model.

Evaluation of the Critical Correlation Length and the Critical Compressibility from fit of the Small *k* Region of the Static Oxygen-Oxygen Structure Factor *S(k)*

Close to a critical point, anomalous fluctuations in density develop, which can be quantified via scattering experiments, visible at small wavevectors, *k*. These fluctuations, i.e. the anomalous component of the structure factor, $S_A(k)$, are properly described by a Lorentzian functional form for $k \to 0$,

$$S_A(k) = \frac{S_A(0)}{1+\xi^2 k^2}$$

to which should be added the standard normal component. $S_A(0)$ is linked to, indeed, is linearly proportional to, the critical component of the compressibility (Eq. 2 in the main text) and $\xi$ measures the static correlation length.

We evaluate the instantaneous value of the structure factor, i.e., structure factor for a configuration, by estimating the Fourier transform of the density

$$\rho_{\vec{k}} = \frac{1}{\sqrt{N}} \sum_{j=1}^{N} e^{i\vec{k}\cdot\vec{r}_j},$$

where *i* is the imaginary unit, $\vec{r}_j$ is the position of the oxygen atom of molecule *j* and *N* is the total number of molecules. The ensemble-averaged structure factor is then evaluated as

$$S(k) = < \rho^*_{\vec{k}} \rho_{\vec{k}} > \qquad \text{(S5)}$$

where the average runs over all configurations and all wavevectors have the same modulus $k = |\vec{k}|$ and the symbol $^*$ indicates the complex conjugate. The boundary conditions determine the possible $|\vec{k}|$ values according to $\vec{k} = \frac{2\pi}{L}(n_x, n_y, n_z)$ where $L$ is the size of the edge of the simulated box and $n_x$, $n_y$, $n_z$ are integers. To evaluate the best-fit values for $S_A(0)$ and $\xi$, we perform a least-square fit limited to $k < 4$ nm$^{-1}$ with the fit function

$$S(k) = a + bk^2 + \frac{S_A(0)}{1+\xi^2 k^2},$$

where the term $a+bk^2$ models standard component of the structure factor at small *k* (*54*). In the fit procedure, weights, which take two independent quantities into account, are assigned to each $S(k)$ value. In the first one, the error is assumed to be proportional to the number of independent $\vec{k}$ having the same modulus. In addition, the error on each data point is considered to be proportional to the relaxation time of $S(\vec{k})$, assuming a $k^2$ dependence.

Indeed, as shown below (subsection on *S(k, t)*), the density-density relaxation time scales with $k^{-2}$ at small *k*. Examples of the fit procedure are reported in Fig. S8.

Fig. S9 shows the inverse of the critical component of the structure factor (defined as $S(k) - (a+bk^2)$ ) as a function of $k^2$. Even at small *k*, a linear fit in $k^2$ provides a high

quality representation of the data, suggesting that corrections to the Lorentzian shape expected at the critical point (*35*) are not visible in the studied *T* interval.

*S(k)* from *g(r)*

To provide an estimate of the quality of the numerical *S*(*k*), we also calculate *S*(*k*) by taking the Fourier transform of the radial distribution function *g*(*r*) (*54*):

$$S(k) = 1 + 4\pi\rho \int_0^\infty [g(r) - 1] \frac{sin(kr)}{kr} r^2 \, dr \quad \text{(S6)}$$

where $\rho$ is the molecule number density. The resulting structure factors are also shown in Fig. S8. In the region of wavevectors accessible to the size of the simulation box *L*, direct calculations of *S*(*k*) in Fourier space (Eq. S5) and *S*(*k*) estimates from transformed real space (Eq. S6) provide the same results.

*S(k,t)*

To properly estimate the error at different *k* in *S*(*k*), we study the *k*-dependence of the correlation time of the collective density fluctuation correlation function

$$S(k,t) = < \rho_{\vec{k}}^*(t) \rho_{\vec{k}}(0) > .$$

Fig. S4(a) shows the time dependence of *S*(*k, t*) for one arbitrary temperature. The behavior of *S*(*k, t*) at small *k* can be quite precisely modeled as a stretched exponential function (*55*), with stretching exponent $\beta = 0.7 \pm 0.1$. The *k*-dependent correlation time, as illustrated in Fig. S4(b), follows a $k^{-2}$ dependence, a characteristic behavior of diffusive processes.

Test of the Equilibration for the *N* =36,424 System

To provide evidence that even the slowest relaxation times have been sufficiently equilibrated, we show the normalized correlation function of the density fluctuations *S*(*k,t*)/*S*(*k,*0) for several low *T* simulations in Fig. S5. Due to the presence of critical fluctuations, the slowest mode is the one with the smallest accessible *k*. For all *T* and all *k*, *S*(*k,t*)/*S*(*k,*0) relaxes to zero on a time scale smaller than the simulated trajectory. The length in time for each trajectory is reported in Table S4.

Correlation Between Density and Structure

To provide evidence that the structural properties of the system are different in the two phases, we compare the oxygen-oxygen radial distribution function *g*(*r*) and the corresponding structure factor *S*(*k*) averaged over different time blocks, centered in different points of the investigated trajectory. In particular, Fig. S2 shows that during the time in which the system prevalently explores low density values, the first shell is very well resolved ($g(r) \approx 0$ for $r \approx 3.2$). In contrast, when the system explores higher densities, there is no clear separation between first and second shells. Similarly, the structure factor pre-peak shifts from 17 to 19 $nm^{-1}$ on going from low to high density (*56*).

Crystallization

To provide evidence that no crystallization occurs in the simulations, we have evaluated the fraction of molecules with crystalline character following two of the most common classification schemes, CHILL+ (*57*) and Russo-Romano-Tanaka (*58*). CHILL+ classifies molecules according to three crystalline structures (cubic ice, hexagonal ice, and clathrate) and two interfacial structures (interfacial ice and interfacial clathrate). The fraction of molecules belonging to these groups as a function of $T$ along the $\rho = 1.012$ g/cm$^3$ isochore are shown in Fig. S3. The fractions of crystalline ices are limited at all $T$ below a few percent. There are about 5% molecules classified as interfacial clathrate and 10% classified as interfacial ice. Both these two classes of molecules show a weak dependence on $T$. None of these classes shows any significant increase with time during the simulated period.

The classification of Russo-Romano-Tanaka (*58*) is designed to eliminate the large fraction of local environments commonly detected as being interfacial ice but that are not wetting a crystalline nucleus, by including information up to the third shell of neighbours in the classification scheme. Here, molecules are classified according to four crystalline structures (cubic and hexagonal ice, ice 0 and clathrate) and just one of interfacial ice species. The fraction of molecules belonging to these groups as a function of $T$ along the $\rho = 1.012$ g/cm$^3$ isochore are shown in Fig. S3. As expected, the Russo-Romano-Tanaka method detects a significantly smaller concentration if ice molecules compared to CHILL+.

**Fig. S1.**

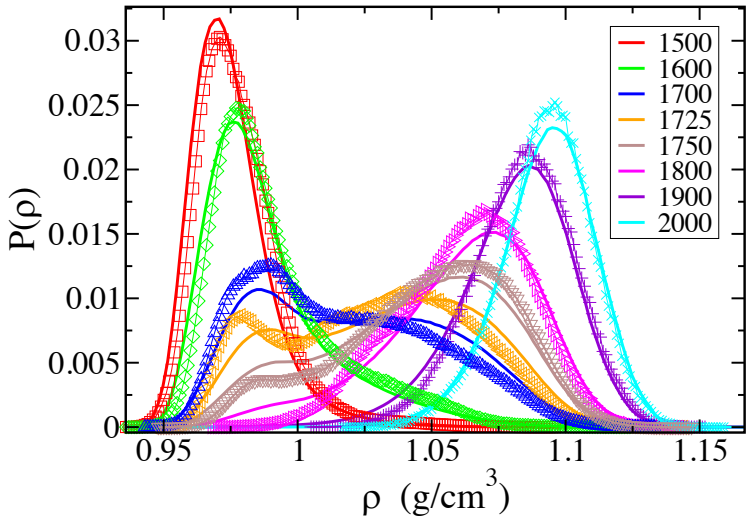


**Comparison of the distribution of density fluctuations**. Density fluctuations observed in individual runs are presented with symbols at T=178 K and multiple pressures (see the legend: pressures in bars) and the corresponding quantities rebuilt from the histogram reweighting technique are presented with lines. Here the model is TIP4P/2005 and N=300.

**Fig. S2**

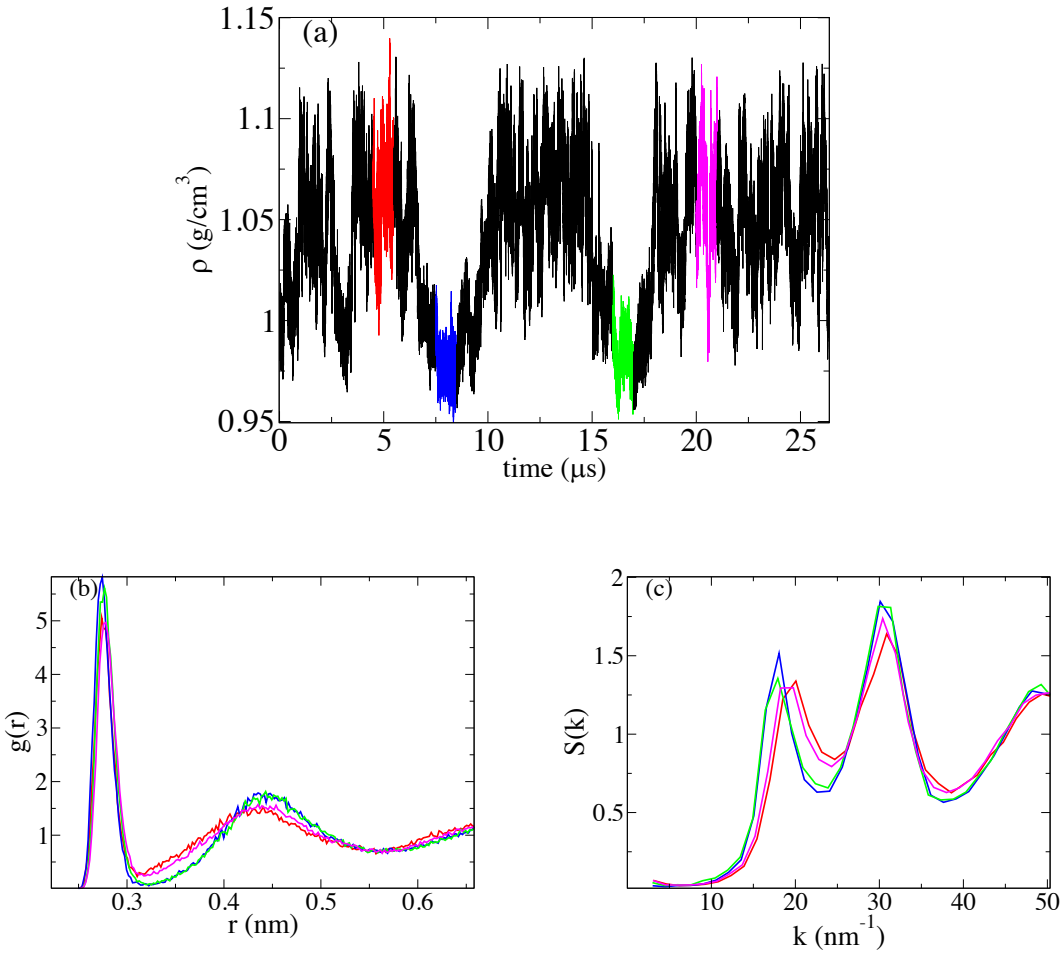


**Correlation between density and structure.** (a) Time dependence of the density at $P$ = 1750 bar, $T$ = 177 K, and N=300 for TIP4P/2005. Four intervals are highlighted by different colors. Two of the intervals are centered at times at which the density assumes large values (red and magenta) and the other two are centered at times at which the density is smallest (blue and green). (b) Oxygen-oxygen radial distribution function $g(r)$, (c) corresponding structure factor $S(k)$ averaged over each colored time block (same color code as in (a)).

**Fig. S3**

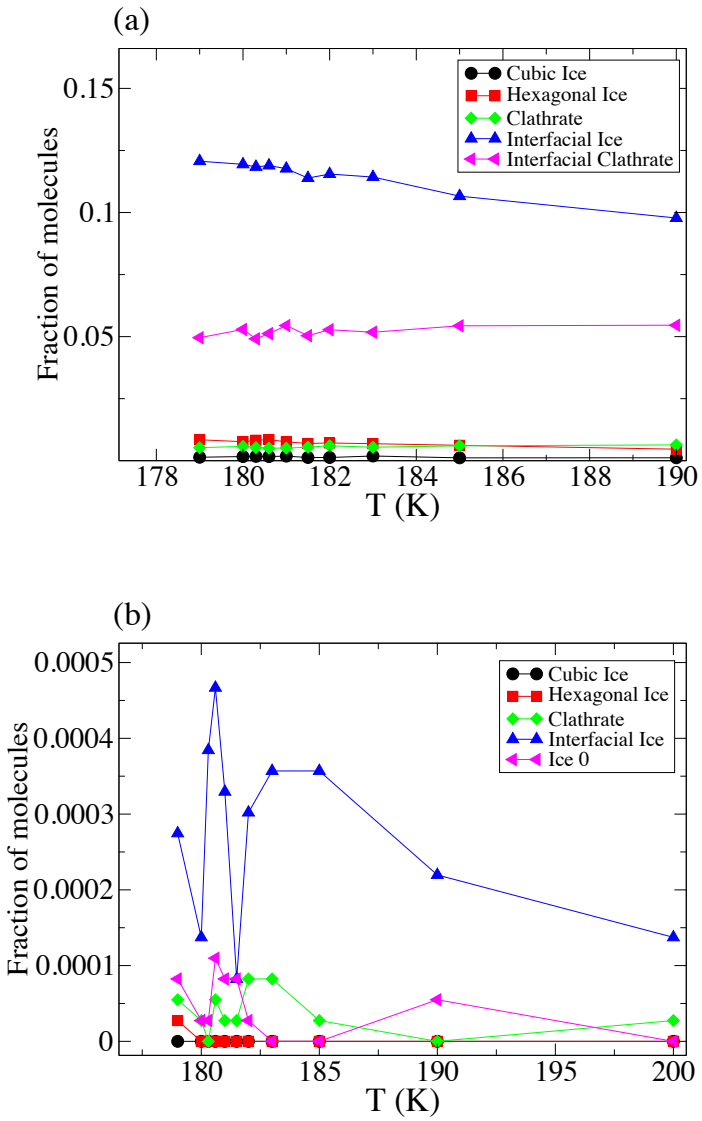


**Crystallization analysis.** Molecules are classified according to (a) the CHILL+ (*57*) and (b) the Russo-Romano-Tanaka (*58*) algorithms. Here the model is TIP4P/2005 and the density is 1.012 g/cm$^3$. Note the small fraction of crystalline particles detected by both methods.

**Fig. S4**

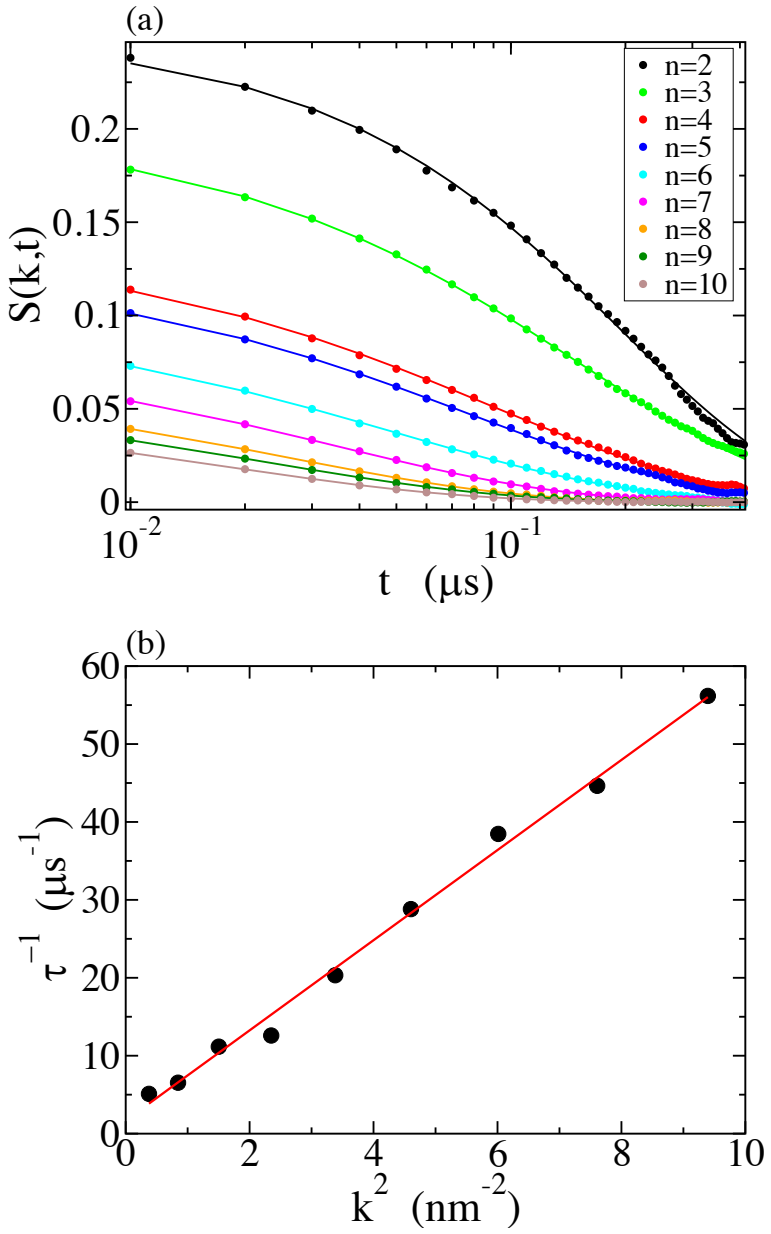


**Time-dependent analysis of density fluctuations.** (a) Symbols indicate $S(k, t)$ for $k = \frac{\pi}{L}n$, with n=2,3...9,10. Lines are fit according to a stretched exponential function. (b) Corresponding $\tau^{-1}$ for each $k^2$. Here the model is TIP4P/2005 and T=183K, $N$ = 36,424, $\rho$ = 1.012 g/cm$^3$.

**Fig. S5**

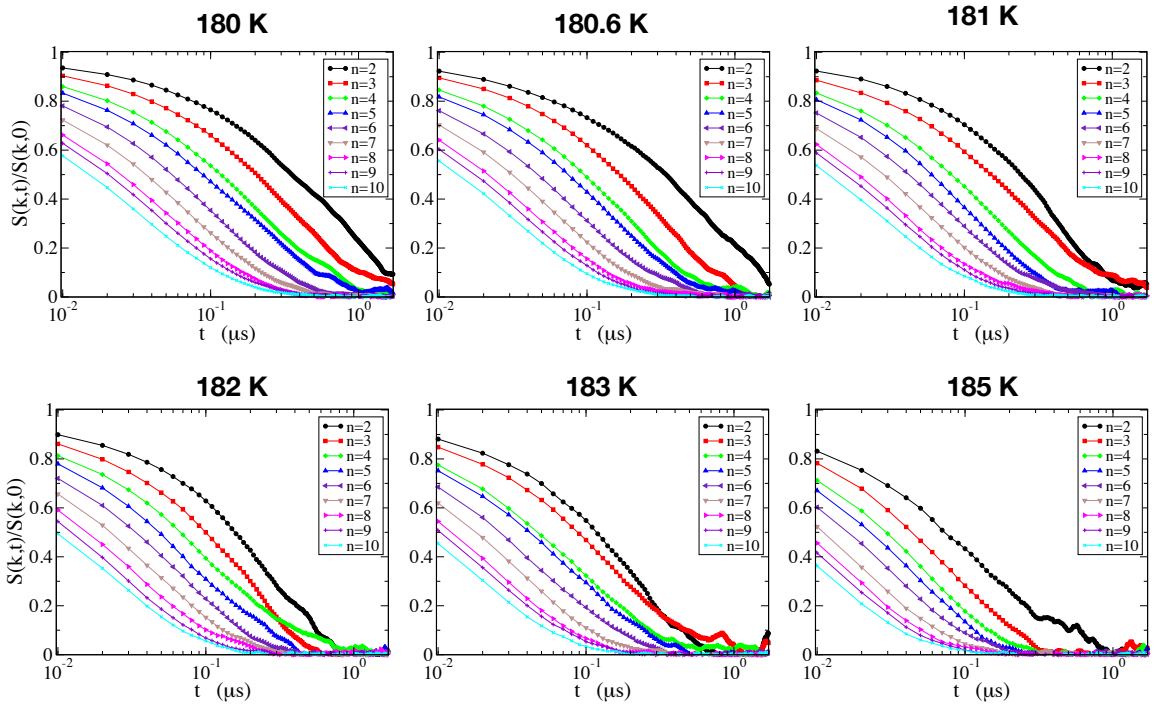


**Time-dependent analysis of density fluctuations for six low temperatures.** Symbols indicate $S(k, t)$ for $k = \frac{\pi}{L}n$, with n=2,3...9,10. Note that, due to periodic boundary conditions, the smallest accessible $k$ is $\frac{2\pi}{L}$, hence the smallest $n$ is 2. The correlation functions are averaged over all $\vec{k}$ with the same $|k|$. Calculations are for TIP4P/2005, $N$ = 36,424, $\rho$ = 1.012 g/cm$^3$.

**Fig. S6**

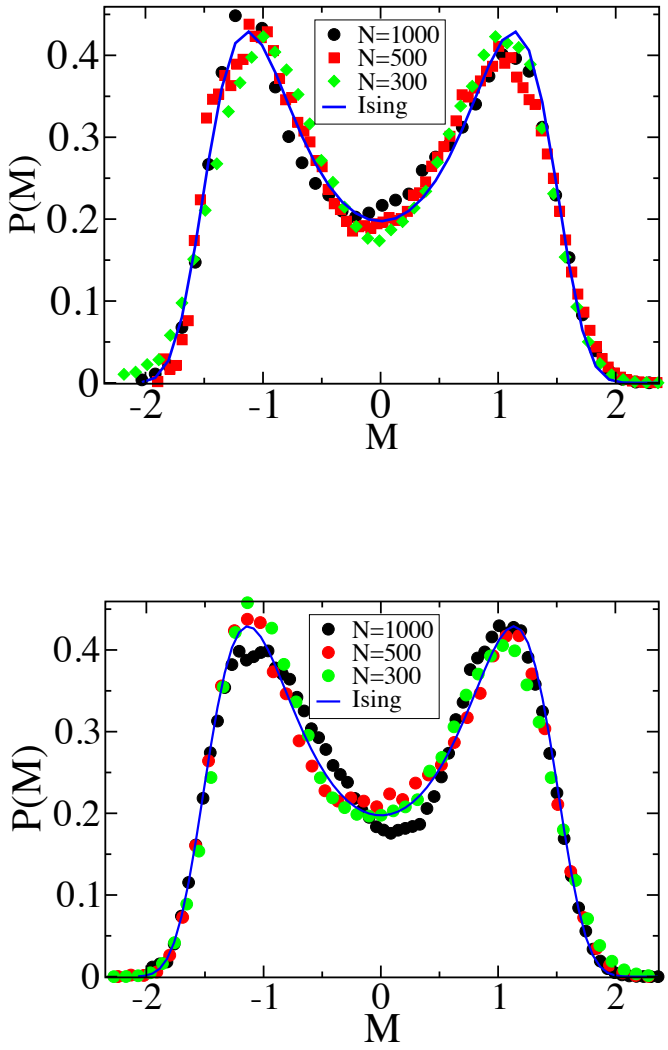


**Ising fit for TIP4P/2005 (top) and TIP4P/Ice (bottom) for small-system sizes studied here.**

**Fig. S7**

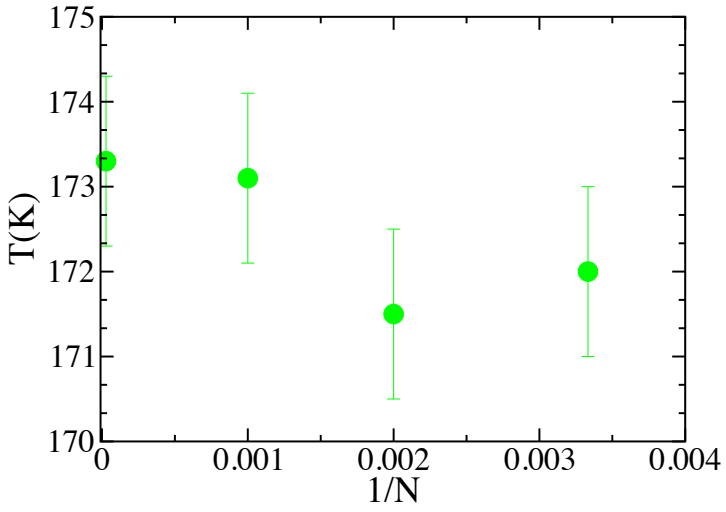


**Critical temperatures evaluated at different sizes for TIP4P/2005 systems.** Bars are estimated systematic errors arising from calculation methods.

**Fig. S8**

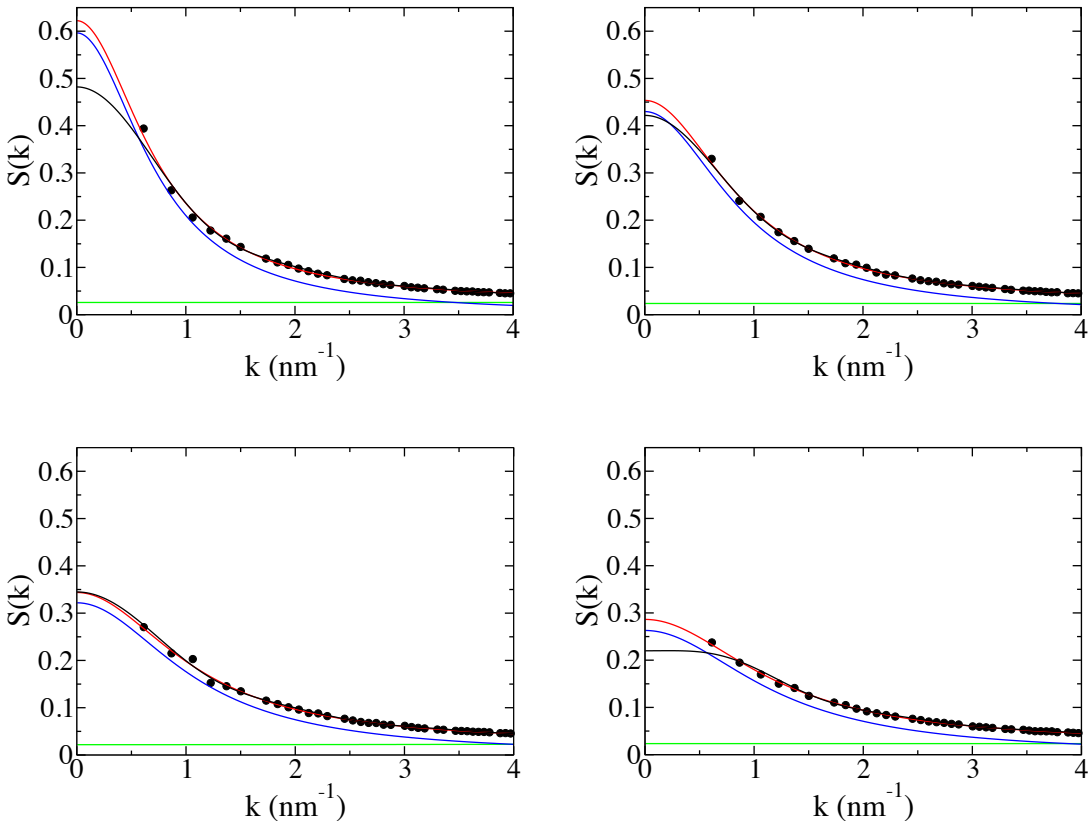


**Structure factor analysis and fits at multiple illustrative temperatures (top-left: T=180.3 K, top-right: T=181 K, bottom-left: T=183 K, bottom-right: T=185 K).** The red curve is the best fit to a normal component (green) plus a Lorentzian (blue) function of the numerical data (filled circles). The black curve is the structure factor as evaluated by the Fourier transform of the radial distribution function. The model is TIP4P/2005 at a density $\rho$ = 1.012 g/cm$^3$.

**Fig. S9**

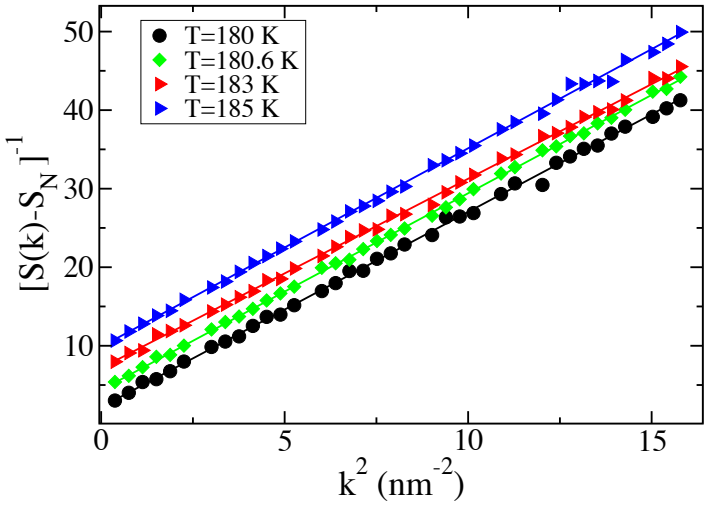


**Inverse of the critical part of the structure factor as a function of $k^2$ for the TIP4P/2005 model at $\rho$ = 1.012 g/cm$^3$.** The straight lines have intercept of $S_A(0)^{-1}$ and slope of $\xi^2/S_A(0)$. For clarity, data at different $T$ have been shifted by 2, 4 and 6 along the y axis.

**Fig. S10**

**A.**

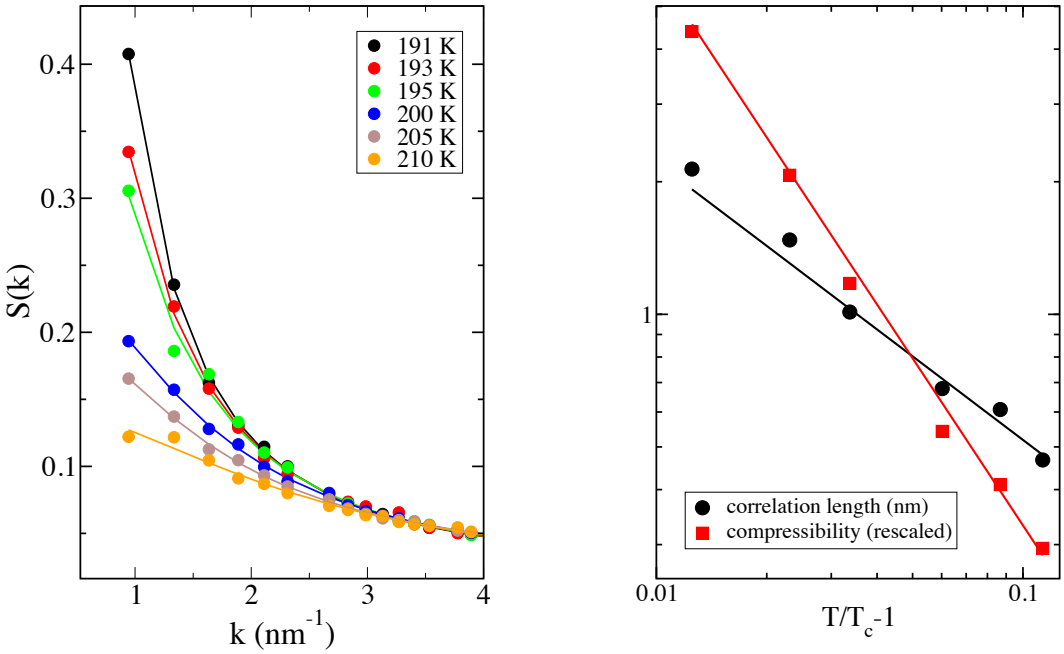


**Anomalous behavior of the structure factor near the critical point of TIP4P/Ice. A.** Low-$k$ region of the structure factor computed for $N$ = 10,000 TIP4P/Ice molecules at different temperatures and a fixed density $\rho$ = 1.015 g/cm$^3$, in close proximity to the critical isochore (see Table S3). **B**. Calculated values of the isothermal compressibility (see main text Eq. 2), in units of Pa$^{-1}$, and scaled by a multiplication factor 2x10$^8$, and the correlation length (see main text Eq. 3). The slope of the lines through the data correspond to the Ising 3-d critical exponents ($\nu = 0.63;\ \gamma = 1.26$), see Eqs. 4, 5 in main text. Critical temperature obtained by a constrained least-squares fit to the data, yielding $T_c$ = 188.6 K.

**Table S1.**

Number of independent runs and total length of TIP4P/2005 runs for each state point (and for each run).

| | | N=300 | | N=500 | | N=1000 | |
|---|---|---|---|---|---|---|---|
| T (K) | P (bar) | runs | time/$\mu$s | runs | time/$\mu$s | runs | time/$\mu$s |
| 177 | 1650 | 1 | 10 | 2 | 80, 90 | 2 | 51, 64 |
| | 1725 | 1 | 29 | | | | |
| | 1700 | | | 3 | 91, 91, 113 | 3 | 50, 65, 51 |
| | 1750 | 1 | 29 | 3 | 80, 95, 112 | 3 | 50, 65, 60 |
| | 1775 | 1 | 20 | | | | |
| | 1800 | | | 3 | 71, 73, 86 | 3 | 40, 77, 67 |
| | 1850 | | | 2 | 94, 90 | 1 | 51 |
| 178 | 1400 | 1 | 12 | | | | |
| | 1500 | 1 | 45 | 1 | 10 | 1 | 10 |
| | 1550 | | | 1 | 10 | 1 | 43 |
| | 1600 | 1 | 25 | 2 | 32, 30 | 3 | 33, 10, 40 |
| | 1650 | 1 | 5 | 3 | 30, 30, 40 | 3 | 33, 10, 30 |
| | 1700 | 1 | 30 | 3 | 35, 30, 40 | 4 | 3, 39, 31, 17 |
| | 1725 | 1 | 33 | | | | |
| | 1750 | 1 | 33 | 2 | 35, 75 | 2 | 31, 29 |
| | 1800 | 1 | 20 | 2 | 30, 72 | 1 | 34 |
| | 1850 | | | 1 | 50 | | |
| | 1900 | 1 | 10 | | | | |
| | 2000 | 1 | 10 | | | | |
| 179 | 1400 | 1 | 20 | | | | |
| | 1500 | 1 | 12 | 2 | 20,42 | | |
| | 1550 | | | 1 | 42 | 1 | 20 |
| | 1575 | | | 1 | 20 | | |
| | 1600 | 1 | 88 | 3 | 11, 40, 40 | 3 | 40, 32, 7 |
| | 1625 | | | | | 1 | 40 |
| | 1650 | 1 | 20 | 3 | 73, 40, 11 | 3 | 43, 7, 7 |
| | 1700 | 1 | 12 | 3 | 72, 11, 10 | 3 | 42,25, 7 |
| | 1750 | 1 | 20 | 1 | 72 | 2 | 40,10 |
| | 1800 | 1 | 8 | 2 | 40,20 | 2 | 31 ,8 |

**Table S2.**

Number of independent runs and total length of TIP4P/Ice runs for each state point (and for each run).

| | | N=300 | | N=500 | | N=1000 | |
|---|---|---|---|---|---|---|---|
| T (K) | P (bar) | runs | time/$\mu$s | runs | time/$\mu$s | runs | time/$\mu$s |
| 188 | 1100 | 1 | 43 | | | | |
| | 1300 | 1 | 43 | | | | |
| | 1500 | 1 | 43 | | | | |
| | 1625 | 1 | 43 | | | | |
| | 1675 | 1 | 43 | | | 1 | 4 |
| | 1725 | 1 | 43 | | | 1 | 6 |
| | 1800 | | | | | 2 | 6,6 |
| | 1850 | 1 | 43 | | | | |
| | 1900 | | | | | 2 | 9,6 |
| | 2000 | 1 | 43 | | | | |
| | 2500 | | | | | 1 | 4 |
| 190 | 1100 | | | 1 | 16 | 1 | 9 |
| | 1300 | 1 | 43 | 1 | 16 | 1 | 9 |
| | 1500 | 1 | 43 | 1 | 38 | 1 | 9 |
| | 1625 | 1 | 43 | | | | |
| | 1650 | 1 | 43 | 1 | 34 | 1 | 9 |
| | 1675 | 1 | 43 | | | | |
| | 1700 | | | 1 | 16 | | |
| | 1725 | 1 | 43 | | | 1 | 15 |
| | 1760 | | | | | 1 | 9 |
| | 1800 | | | 1 | 9 | 1 | 8 |
| | 1850 | 1 | 43 | | | | |
| | 1900 | | | | | 1 | 9 |
| | 2000 | 1 | 43 | 1 | 9 | 1 | 9 |
| 191 | 1600 | | | | | 1 | 40 |
| | 1650 | | | | | 2 | 54, 50 |
| | 1675 | | | | | 1 | 46 |
| | 1700 | | | | | 1 | 53 |
| | 1750 | | | | | 1 | 49 |
| | 1800 | | | | | 1 | 35 |
| | 1850 | | | | | 1 | 29 |
| | 1900 | | | | | 1 | 19 |
| 192 | 1100 | 1 | 30 | 1 | 12 | | |
| | 1300 | 1 | 30 | 1 | 15 | | |
| | 1500 | 1 | 30 | 1 | 28 | | |
| | 1550 | | | | | 1 | 30 |
| | 1600 | | | | | 1 | 12 |
| | 1625 | 1 | 41 | 1 | 25 | | |
| | 1650 | | | 1 | 30 | 1 | 35 |
| | 1675 | 1 | 25 | | | | |
| | 1700 | | | 1 | 30 | 1 | 13 |
| | 1725 | 1 | 40 | | | | |
| | 1750 | | | | | 1 | 22 |
| | 1800 | | | 1 | 10 | | |
| | 1850 | 1 | 28 | | | | |
| | 1900 | | | | | 1 | 16 |
| | 2000 | 1 | 18 | 1 | 8 | 1 | 5 |

**Table S3.**

Critical parameters calculated from the simulations.

| | TIP4P/2005 | | | | TIP4P/Ice | | | |
|---|---|---|---|---|---|---|---|---|
| $N$ | $T_c$ (K) | $P_c$ (bar) | $s$ (kg mol/m$^3$ kJ) | $\rho_c$ (g/cm$^3$) | $T_c$ (K) | $P_c$ (bar) | $s$ (kg mol/m$^3$ kJ) | $\rho_c$ (g/cm$^3$) |
| 300 | 172.0 | 1861 | 96.0 | 1.039 | 188.6 | 1725 | 83.3 | 1.017 |
| 500 | 171.5 | 1872 | 75.1 | 1.024 | 188.1 | 1746 | 86.7 | 1.015 |
| 1000 | 173.1 | 1850 | 73.1 | 1.028 | 188.6 | 1746 | 82.3 | 1.012 |
| 10000 | | | | | 188.6 | | | |
| 36424 | 173.3 | | | | | | | |

**Table S4.**

Length of large box simulations for scattering analysis of TIP4P/2005 ($N$ = 36,424) and TIP4P/ICE ($N$ = 10,000).

| TIP4P/2005 | | TIP4P/ICE | |
|---|---|---|---|
| T (K) | time/$\mu$s | T (K) | time/$\mu$s |
| 180 | 30.1 | 191 | 17.4 |
| 180.3 | 21.7 | 193 | 5.0 |
| 180.6 | 25.4 | 195 | 4.4 |
| 181 | 17.4 | 200 | 4.1 |
| 181.5 | 10.2 | 205 | 3.6 |
| 182 | 7.7 | 210 | 2.3 |
| 183 | 10.1 | | |
| 185 | 9.0 | | |
| 190 | 3.2 | | |
| 200 | 4.5 | | |
| 250 | 1.0 | | |
| 300 | 1.0 | | |

**References and Notes**


1. F. Franks, *Water: A Matrix for Life* (RSC Paperbacks, Royal Society of Chemistry, ed. 2, 2000).

2. P. Ball, Water is an active matrix of life for cell and molecular biology. *Proc. Natl. Acad. Sci. U.S.A.* **114**, 13327–13335 (2017). doi:10.1073/pnas.1703781114 Medline

3. C. G. Salzmann, Advances in the experimental exploration of water's phase diagram. *J. Chem. Phys.* **150**, 060901 (2019). doi:10.1063/1.5085163 Medline

4. F. H. Stillinger, Water revisited. *Science* **209**, 451–457 (1980). doi:10.1126/science.209.4455.451 Medline

5. J. Russo, K. Akahane, H. Tanaka, Water-like anomalies as a function of tetrahedrality. *Proc. Natl. Acad. Sci. U.S.A.* **115**, E3333–E3341 (2018). doi:10.1073/pnas.1722339115 Medline

6. H. E. Stanley, J. Teixeira, Interpretation of the unusual behavior of $H_2O$ and $D_2O$ at low temperatures: Tests of a percolation model. *J. Chem. Phys.* **73**, 3404–3422 (1980). doi:10.1063/1.440538

7. P. G. Debenedetti, Supercooled and glassy water. *J. Phys. Condens. Matter* **15**, R1669–R1726 (2003). doi:10.1088/0953-8984/15/45/R01

8. R. J. Speedy, C. A. Angell, Isothermal compressibility of supercooled water and evidence for a thermodynamic singularity at −45°C. *J. Chem. Phys.* **65**, 851–858 (1976). doi:10.1063/1.433153

9. S. Sastry, P. G. Debenedetti, F. Sciortino, H. E. Stanley, Singularity-free interpretation of the thermodynamics of supercooled water. *Phys. Rev. E* **53**, 6144–6154 (1996). doi:10.1103/PhysRevE.53.6144 Medline

10. P. H. Handle, T. Loerting, F. Sciortino, Supercooled and glassy water: Metastable liquid(s), amorphous solid(s), and a no-man's land. *Proc. Natl. Acad. Sci. U.S.A.* **114**, 13336–13344 (2017). doi:10.1073/pnas.1700103114 Medline

11. N. J. Hestand, J. L. Skinner, Perspective: Crossing the Widom line in no man's land: Experiments, simulations, and the location of the liquid-liquid critical point in supercooled water. *J. Chem. Phys.* **149**, 140901 (2018). doi:10.1063/1.5046687 Medline

12. J. A. Sellberg, C. Huang, T. A. McQueen, N. D. Loh, H. Laksmono, D. Schlesinger, R. G. Sierra, D. Nordlund, C. Y. Hampton, D. Starodub, D. P. DePonte, M. Beye, C. Chen, A. V. Martin, A. Barty, K. T. Wikfeldt, T. M. Weiss, C. Caronna, J. Feldkamp, L. B. Skinner, M. M. Seibert, M. Messerschmidt, G. J. Williams, S. Boutet, L. G. M. Pettersson, M. J. Bogan, A. Nilsson, Ultrafast X-ray probing of water structure below the homogeneous ice nucleation temperature. *Nature* **510**, 381–384 (2014). doi:10.1038/nature13266 Medline

13. K. H. Kim, A. Späh, H. Pathak, F. Perakis, D. Mariedahl, K. Amann-Winkel, J. A. Sellberg, J. H. Lee, S. Kim, J. Park, K. H. Nam, T. Katayama, A. Nilsson, Maxima in the thermodynamic response and correlation functions of deeply supercooled water. *Science* **358**, 1589–1593 (2017). doi:10.1126/science.aap8269 Medline

14. G. Pallares, M. El Mekki Azouzi, M. A. González, J. L. Aragones, J. L. F. Abascal, C. Valeriani, F. Caupin, Anomalies in bulk supercooled water at negative pressure. *Proc. Natl. Acad. Sci. U.S.A.* **111**, 7936–7941 (2014). doi:10.1073/pnas.1323366111 Medline

15. K. Amann-Winkel, C. Gainaru, P. H. Handle, M. Seidl, H. Nelson, R. Böhmer, T. Loerting, Water's second glass transition. *Proc. Natl. Acad. Sci. U.S.A.* **110**, 17720–17725 (2013). doi:10.1073/pnas.1311718110 Medline

16. P. H. Poole, F. Sciortino, U. Essmann, H. E. Stanley, Phase behavior of metastable water. *Nature* **360**, 324–328 (1992). doi:10.1038/360324a0

17. A. K. Soper, Is water one liquid or two? *J. Chem. Phys.* **150**, 234503 (2019). doi:10.1063/1.5096460 Medline

18. O. Mishima, H. E. Stanley, Decompression-induced melting of ice IV and the liquid-liquid transition in water. *Nature* **392**, 164–168 (1998). doi:10.1038/32386

19. S. Woutersen, B. Ensing, M. Hilbers, Z. Zhao, C. A. Angell, A liquid-liquid transition in supercooled aqueous solution related to the HDA-LDA transition. *Science* **359**, 1127–1131 (2018). doi:10.1126/science.aao7049 Medline

20. J. C. Palmer, P. H. Poole, F. Sciortino, P. G. Debenedetti, Advances in computational studies of the liquid-liquid transition in water and water-like models. *Chem. Rev.* **118**, 9129–9151 (2018). doi:10.1021/acs.chemrev.8b00228 Medline

21. J. C. Palmer, R. S. Singh, R. Chen, F. Martelli, P. G. Debenedetti, Density and bond-orientational relaxations in supercooled water. *Mol. Phys.* **114**, 2580–2585 (2016). doi:10.1080/00268976.2016.1179351

22. E. B. Moore, V. Molinero, Structural transformation in supercooled water controls the crystallization rate of ice. *Nature* **479**, 506–508 (2011). doi:10.1038/nature10586 Medline

23. Y. Li, J. Li, F. Wang, Liquid-liquid transition in supercooled water suggested by microsecond simulations. *Proc. Natl. Acad. Sci. U.S.A.* **110**, 12209–12212 (2013). doi:10.1073/pnas.1309042110 Medline

24. Y. Ni, J. L. Skinner, Evidence for a liquid-liquid critical point in supercooled water within the E3B3 model and a possible interpretation of the kink in the homogeneous nucleation line. *J. Chem. Phys.* **144**, 214501 (2016). doi:10.1063/1.4952991 Medline

25. J. C. Palmer, F. Martelli, Y. Liu, R. Car, A. Z. Panagiotopoulos, P. G. Debenedetti, Metastable liquid-liquid transition in a molecular model of water. *Nature* **510**, 385–388 (2014). doi:10.1038/nature13405 Medline

26. F. Sciortino, I. Saika-Voivod, P. H. Poole, Study of the ST2 model of water close to the liquid-liquid critical point. *Phys. Chem. Chem. Phys.* **13**, 19759–19764 (2011). doi:10.1039/c1cp22316j Medline

27. T. A. Kesselring, G. Franzese, S. V. Buldyrev, H. J. Herrmann, H. E. Stanley, Nanoscale dynamics of phase flipping in water near its hypothesized liquid-liquid critical point. *Sci. Rep.* **2**, 474 (2012). doi:10.1038/srep00474 Medline

28. Y. Liu, J. C. Palmer, A. Z. Panagiotopoulos, P. G. Debenedetti, Liquid-liquid transition in ST2 water. *J. Chem. Phys.* **137**, 214505 (2012). doi:10.1063/1.4769126 Medline

29. A. M. Ferrenberg, R. H. Swendsen, Optimized Monte Carlo data analysis. *Phys. Rev. Lett.* **63**, 1195–1198 (1989). doi:10.1103/PhysRevLett.63.1195 Medline

30. J. L. F. Abascal, C. Vega, A general purpose model for the condensed phases of water: TIP4P/2005. *J. Chem. Phys.* **123**, 234505 (2005). doi:10.1063/1.2121687 Medline

31. J. L. F. Abascal, E. Sanz, R. García Fernández, C. Vega, A potential model for the study of ices and amorphous water: TIP4P/Ice. *J. Chem. Phys.* **122**, 234511 (2005). doi:10.1063/1.1931662 Medline

32. N. B. Wilding, A. D. Bruce, Density fluctuations and field mixing in the critical fluid. *J. Phys. Condens. Matter* **4**, 3087–3108 (1992). doi:10.1088/0953-8984/4/12/008

33. J. Guo, R. S. Singh, J. C. Palmer, Anomalous scattering in supercooled ST2 water. *Mol. Phys.* **116**, 1953–1964 (2018). doi:10.1080/00268976.2018.1442595

34. L. S. Ornstein, F. Zernike, Accidental deviations of density and opalescence at the critical point of a single substance. *Proc. Sect. Sci. K Ned. Akad. Wet.* **17**, 793 (1914).

35. M. E. Fisher, Correlation functions and the critical region of simple fluids. *J. Math. Phys.* **5**, 944–962 (1964). doi:10.1063/1.1704197

36. H. E. Stanley, *Introduction to Phase Transitions and Critical Phenomena* (Oxford Univ. Press, 1971).

37. J. V. Sengers, J. M. H. L. Sengers, Thermodynamic behavior of fluids near the critical point. *Annu. Rev. Phys. Chem.* **37**, 189–222 (1986). doi:10.1146/annurev.pc.37.100186.001201

38. K. Binder, Simulations clarify when supercooled water freezes into glassy structures. *Proc. Natl. Acad. Sci. U.S.A.* **111**, 9374–9375 (2014). doi:10.1073/pnas.1408908111 Medline

39. R. Kurita, H. Tanaka, Drastic enhancement of crystal nucleation in a molecular liquid by its liquid-liquid transition. *Proc. Natl. Acad. Sci. U.S.A.* **116**, 24949–24955 (2019). doi:10.1073/pnas.1909660116 Medline

40. G. A. Cisneros, K. T. Wikfeldt, L. Ojamäe, J. Lu, Y. Xu, H. Torabifard, A. P. Bartók, G. Csányi, V. Molinero, F. Paesani, Modeling molecular interactions in water: From pairwise to many-body potential energy functions. *Chem. Rev.* **116**, 7501–7528 (2016). doi:10.1021/acs.chemrev.5b00644 Medline

41. B. Cheng, E. A. Engel, J. Behler, C. Dellago, M. Ceriotti, Ab initio thermodynamics of liquid and solid water. *Proc. Natl. Acad. Sci. U.S.A.* **116**, 1110–1115 (2019). doi:10.1073/pnas.1815117116 Medline

42. P. G. Debenedetti, F. Sciortino, G. H. Zerze, Data for "Second critical point in two realistic models of water," Version 1, Zenodo (2020); https://doi.org/10.5281/zenodo.3836542.

43. H. J. Berendsen, D. van der Spoel, R. van Drunen, GROMACS: A message-passing parallel molecular dynamics implementation. *Comput. Phys. Commun.* **91**, 43–56 (1995). doi:10.1016/0010-4655(95)00042-E

44. B. Hess, C. Kutzner, D. van der Spoel, E. Lindahl, GROMACS 4: Algorithms for highly efficient, load-balanced, and scalable molecular simulation. *J. Chem. Theory Comput.* **4**, 435–447 (2008). doi:10.1021/ct700301q Medline

45. U. Essmann, L. Perera, M. L. Berkowitz, T. Darden, H. Lee, L. G. Pedersen, A smooth particle mesh Ewald method. *J. Chem. Phys.* **103**, 8577–8593 (1995). doi:10.1063/1.470117

46. J. L. F. Abascal, C. Vega, Widom line and the liquid-liquid critical point for the TIP4P/2005 water model. *J. Chem. Phys.* **133**, 234502 (2010). doi:10.1063/1.3506860 Medline

47. S. Kumar, J. M. Rosenberg, D. Bouzida, R. H. Swendsen, P. A. Kollman, The weighted histogram analysis method for free-energy calculations on biomolecules. I. The method. *J. Comput. Chem.* **13**, 1011–1021 (1992). doi:10.1002/jcc.540130812

48. S. Fishman, M. E. Fisher, Critical point scaling in the Percus-Yevick equation. *Physica A* **108**, 1–13 (1981). doi:10.1016/0378-4371(81)90161-8

49. M. Bonetti, P. Calmettes, C. Bervillier, Small-angle neutron scattering from supercritical heavy water at off-critical densities. *J. Chem. Phys.* **115**, 4660–4669 (2001). doi:10.1063/1.1392362

50. R. S. Singh, J. W. Biddle, P. G. Debenedetti, M. A. Anisimov, Two-state thermodynamics and the possibility of a liquid-liquid phase transition in supercooled TIP4P/2005 water. *J. Chem. Phys.* **144**, 144504 (2016). doi:10.1063/1.4944986 Medline

51. A. Z. Panagiotopoulos, Monte Carlo methods for phase equilibria of fluids. *J. Phys. Condens. Matter* **12**, R25–R52 (2000). doi:10.1088/0953-8984/12/3/201

52. V. Bianco, G. Franzese, Critical behavior of a water monolayer under hydrophobic confinement. *Sci. Rep.* **4**, 4440 (2014). doi:10.1038/srep04440 Medline

53. M. M. Tsypin, H. W. Blöte, Probability distribution of the order parameter for the three-dimensional ising-model universality class: A high-precision monte carlo study. *Phys. Rev. E* **62**, 73–76 (2000). doi:10.1103/PhysRevE.62.73 Medline

54. J.-P. Hansen, I. R. McDonald, *Theory of Simple Liquids: With Applications to Soft Matter* (Academic Press, ed. 4, 2013).

55. P. G. Debenedetti, F. H. Stillinger, Supercooled liquids and the glass transition. *Nature* **410**, 259–267 (2001). doi:10.1038/35065704 Medline

56. R. Shi, H. Tanaka, Direct evidence in the scattering function for the coexistence of two types of local structures in liquid water. *J. Am. Chem. Soc.* **142**, 2868–2875 (2020). doi:10.1021/jacs.9b11211 Medline

57. A. H. Nguyen, V. Molinero, Identification of clathrate hydrates, hexagonal ice, cubic ice, and liquid water in simulations: The CHILL+ algorithm. *J. Phys. Chem. B* **119**, 9369–9376 (2015). doi:10.1021/jp510289t Medline

58. J. Russo, F. Romano, H. Tanaka, New metastable form of ice and its role in the homogeneous crystallization of water. *Nat. Mater.* **13**, 733–739 (2014). doi:10.1038/nmat3977 Medline